

Amplifying state dissimilarity leads to robust and interpretable clustering of scientific data

Brooke E. Husic,^{1, a)} Kristy L. Schlueter-Kuck,² and John O. Dabiri^{2,3, b)}

¹⁾Department of Chemistry, Stanford University, Stanford CA 94305, USA

²⁾Department of Mechanical Engineering, Stanford University, Stanford CA 94305, USA

³⁾Department of Civil and Environmental Engineering, Stanford University, Stanford CA 94305, USA

Existing methods that aim to automatically cluster data into physically meaningful subsets typically require assumptions regarding the number, size, or shape of the coherent subgroups. We present a new method, simultaneous Coherent Structure Coloring (sCSC), which accomplishes the task of unsupervised clustering without *a priori* guidance regarding the underlying structure of the data. Rather than directly clustering the states that are most similar, sCSC efficiently separates the most dissimilar states in the system. Specifically, a generalized eigenvalue problem is solved based on the pairwise dissimilarity between the states in the system to be clustered. The set of orthogonal eigenvector solutions is then applied sequentially to the data, leading a converged, binary tree representation of the system. The number of clusters in the data emerges naturally from the tree as the number of its converged branches, and the interrelationship between the clusters is quantified by the branch lengths. To illustrate the versatility of the method, we apply it to frontier physics problems at vastly different temporal and spatial scales: in a theoretical model of geophysical fluid dynamics, in laboratory measurements of vortex ring formation and entrainment, and in atomistic simulation of the Protein G system. The theoretical flow involves sparse sampling of non-equilibrium dynamics, where this new technique can find and characterize the structures that govern fluid transport using two orders of magnitude less data than required by existing methods. Application of the method to empirical measurements of vortex formation leads to the discovery of a well defined region in which vortex ring entrainment occurs, with potential implications ranging from flow control to cardiovascular diagnostics. Finally, the protein folding example demonstrates a data-rich application governed by equilibrium dynamics, where the technique in this manuscript automatically discovers the hierarchy of distinct processes that govern protein folding and clusters protein configurations accordingly. We anticipate straightforward translation to many other fields where existing analysis tools, such as *k*-means and traditional hierarchical clustering, require ad hoc assumptions on the data structure or lack the interpretability of the present method. The method is also potentially generalizable to fields where the underlying processes are less accessible, such as genomics and neuroscience.

POPULAR SUMMARY

A first step in the exploration of scientific datasets is often a search for underlying structure related to the salient physical, chemical or biological processes. Commonly used tools for unsupervised data clustering impose assumptions such as the number, shape, and size of coherent clusters, while typically lacking insight regarding the relationship among coherent states. In this paper, we show that by amplifying the differences between the states in a dataset, the underlying structure of similar features is revealed naturally, through a converged tree-based representation. Examples ranging from ocean transport and empirical vortex ring measurements to protein folding simulations demonstrate that the method can achieve interpretable clustering of rich or sparse datasets with limited computational expense. The method is potentially generalizable to fields where the underlying processes are less accessible, such as genomics and neuroscience.

INTRODUCTION

Modern science increasingly leverages machine learning on large datasets, from electronic structure to whole genome sequences to distributed ocean sensor measurements. Many of these datasets capture the dynamics of a system evolving in time, encoding trends with predictive power. In other cases, the data represents an amalgam of coexisting equilibrium states that can be parsed to understand the spectrum of physically realizable states of the underlying system. Analyzing these datasets using a statistically robust and interpretable framework is a longstanding challenge that often involves clustering, or the unsupervised learning of coherent groups within the data set.

Clustering is a notoriously challenging problem, in part because there exists no application-agnostic measure of quality or appropriateness¹. Thus, many classes of clustering algorithms have been developed for different problems. Some commonly used techniques include partition-based methods such as *k*-means², or their fuzzy counterparts³; density-based methods such as DBSCAN⁴; and connectivity-based methods such as divisive and agglomerative hierarchical clustering^{5,6}. Regardless of the con-

^{a)}Electronic mail: bhusic@stanford.edu

^{b)}Electronic mail: jodabiri@stanford.edu

ceptual approach, the notion of similarity or dissimilarity as well as the output of the clustering model must be interpretable in the context of the specific application⁷.

Each of the aforementioned methods presents difficulties in this regard. For example, partition-based clustering such as k -means requires a priori knowledge of the number of partitions in a dataset. If multiple results are obtained from different values of k , these results are not interrelated; similarly, the model cannot be used to determine relationships between the k clusters of a single model. While connectivity-based methods feature inter-related clusters, these also require the determination of where to cut the corresponding dendrogram to obtain the clustering result. Although density-based methods do not require a priori or a posteriori determination of the number of clusters to use, these methods are not robust to datasets containing a range of cluster densities⁸.

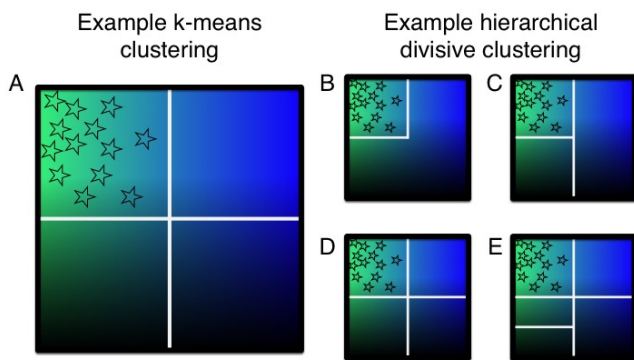


FIG. 1. Conceptual illustration of existing tools for unsupervised data clustering. The observed system comprises a horizontal gradient in color from green to blue, a vertical gradient in brightness from dark to light, and a collection of stars at the upper left. k -means clustering applied to the system, with a specified value $k = 4$, can isolate the stars at the upper left, but cannot simultaneously extract the color or brightness gradients (panel A). Moreover, the method provides no information regarding relationships among the identified clusters. Divisive hierarchical clustering (panels B-E) can separate more of the system, but the requirement of cluster splitting at each level leads to spurious divisions such as the one at the lower left quadrant in panel E.

To conceptually contrast k -means and hierarchical clustering, consider the notional system illustrated in figure 1, which comprises gradients in color and brightness as well as the presence of stars in the upper left corner. Application of k -means clustering might produce four clusters, partitioning along color, brightness, and the presence of stars. However, this result has two drawbacks: first, it requires choosing the number of clusters in advance, where in more complex examples the number of clusters will be unknown; and second, we cannot assess the relationships among the clusters.

Alternatively, we can investigate arbitrary numbers of interrelated clusters by applying divisive hierarchical clustering, wherein the model produces a hierarchical re-

lationship among the groups of states that are split at each level. However, this model requires selection of the point at which to stop dividing clusters. It also has the more nuanced drawback that it can only split an existing cluster, and therefore cannot create a division that crosses multiple existing clusters. Furthermore, since the number of possible divisions scales with the number of existing clusters c as $2^{c-1} - 1$, such algorithms are not feasible for large numbers of clusters unless the initial dataset is sparse⁹ or when a restrictive protocol is used to determine which state to divide⁶.

Here, we present a new method, simultaneous Coherent Structure Coloring (sCSC), which addresses these and other limitations of existing methods by a counter-intuitive focus solely on efficient separation of the most dissimilar states in the system, rather than intentionally clustering the states that are most similar. The end result is a quantitative structure that captures the clusters in the dataset and their interrelationships, without a priori knowledge of the system or ad hoc interpretation of the associated dendrogram. The method is demonstrated in theoretical, experimental, and computational applications ranging from geophysical fluid dynamics to atomistic protein folding, illustrating the broad reach of the technique for equilibrium and nonequilibrium systems, and for both rich and sparse datasets.

SIMULTANEOUS COHERENT STRUCTURE COLORING (sCSC)

Many of the datasets we wish to explore are generated by complex dynamical systems that exhibit instabilities and chaos. A key consequence of these processes is that states of the system (e.g. fluid particle trajectories or protein conformations in the examples below) that are proximal but belonging to different coherent sets will separate exponentially faster as the system evolves than states belonging to the same cluster^{10,11}. On this basis, we hypothesized that complex datasets can be clustered more robustly and effectively by amplifying state differences rather than state similarity. The rationale for this approach is that the exponential separation of dissimilar states can provide more sensitive detection of clusters than a focus on state similarity, the latter requiring longer observation to become apparent^{10,11}. In other words, we aim to identify coherent clusters indirectly, by prioritizing the separation of states with greatest dissimilarity and confidently ruling out the possibility of their membership in the same cluster. Those states that remain together after the separation process will subsequently emerge as belonging to the same cluster.

To amplify the dissimilarity between states, we solve an optimization problem to maximize a figure of merit z that quantifies total state dissimilarity in the dataset. Specifically, this figure of merit depends on a scalar value x_i assigned to each state i in the system, where the squared difference in the scalar value assigned to each of pair

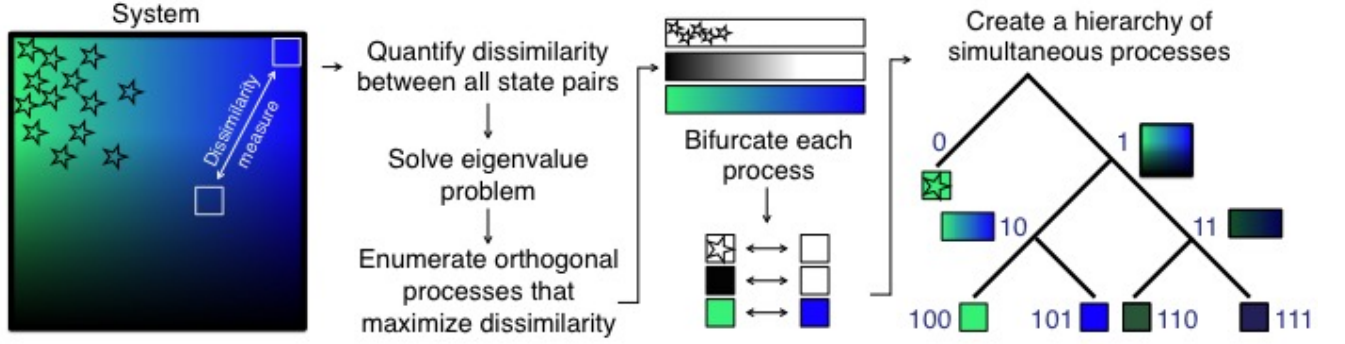


FIG. 2. Conceptual scheme illustrating the sCSC algorithm. First, the dissimilarity between all pairs of states are tabulated in an adjacency matrix. For this example system, states are represented by a uniform grid of squares, two of which are shown for illustration in the left panel. The adjacency matrix is then used to solve an eigenvalue problem in equation 2 that maximizes the dissimilarity measure. The solutions to the eigenvalue problem identify orthogonal processes in the system; in this case, we have stars \leftrightarrow no stars, bright \leftrightarrow dark, and green \leftrightarrow blue. These three processes are bifurcated into two extremes (middle panel). Then, each state is encoded according to each bifurcation. For the first orthogonal process (stars \leftrightarrow no stars), we bifurcate the entire system. For the next orthogonal process (bright \leftrightarrow dark), we bifurcate the system separately and illustrate only states which become bifurcated along this division. For example, there is no state that contains stars and is dark, so branch 0 of the corresponding dendrogram is not further bifurcated. Finally, we bifurcate both branches 10 and 11 according to green or blue.

states (e.g. $(x_1 - x_2)^2$ for states 1 and 2) is weighted by a measure of their dissimilarity. Formally, the clustering parameter z is given by

$$z \equiv \frac{1}{2} \sum_i^n \sum_j^n (x_i - x_j)^2 a_{ij}, \quad (1)$$

where the summations of i and j are each taken over the full set of n states to be clustered, and a_{ij} is an element of the adjacency matrix A containing the pairwise dissimilarity between states i and j . Example definitions of the pairwise dissimilarity can include the standard deviation for comparison of time-dependent signals, or the Jensen-Shannon divergence for comparison of probability distributions¹². Both of these measures will be demonstrated in the applications that follow.

Given the adjacency matrix A , we seek to find state assignments x_i that will maximize z , subject to the constraint that the magnitude of the $n \times 1$ vector X containing the n scalar values x_i must remain finite (e.g. to avoid the trivial case that maximizes z for $x_1 = \infty$ and $x_2 = -\infty$). It is straightforward to show that the constrained optimization of equation 1 with finite X can be written as the generalized eigenvalue problem^{13,14}:

$$LX = \lambda DX, \quad (2)$$

where D is a diagonal matrix with entries equal to the row-sums of the adjacency matrix, i.e. $\sum_j a_{ij}$ for each row i , and $L = D - A$ is the graph Laplacian.

Each of the n eigenvectors X_n of equation 2 represents a solution that assigns to each state a scalar value x_i based on its dissimilarity to the other states in the

system. Those states with scalar assignments in each X that are most dissimilar can be presumed to belong to different clusters of the data when the data is partitioned according to that particular solution of equation 1. The eigenvector X_1 associated with the maximum eigenvalue λ_1 contains the scalar assignments x_i that maximize the figure of merit z . This can be considered the single most effective partitioning of the dataset. Given the analogy between this approach and the problem of fuzzy graph coloring¹⁵, wherein the connected nodes of a graph with large weights are assigned the most disparate values, we call this method Coherent Structure Coloring (CSC)¹⁶. The technique has recently been demonstrated to successfully identify coherent eddies and jets associated with individual fluid particle trajectories in model geophysical flows¹⁷.

A key limitation of the original CSC method¹⁶ is that it relies on only a single eigenvector associated with the largest eigenvalue of equation 2. Hence the method cannot simultaneously distinguish between multiple types of dissimilarity in a dataset (e.g. color and brightness in figure 1), whereas multiple dimensions of dissimilarity are almost always present in real data. Moreover, the method applied to individual fluid particle trajectories¹⁷ relies on a subjectively defined threshold to calculate eigenspace distances, and it was shown to produce degenerate results for fluid particles in chaotic regions of the flow (cf. figure 7 in¹⁷).

Importantly, because the matrix A is real and symmetric, the remaining eigenvectors associated with lesser eigenvalues provide additional, linearly independent (i.e. orthogonal) solutions for partitioning the data, albeit less effectively¹⁸. The key innovation of the present work is to use all of the eigenvectors in a top-down fash-

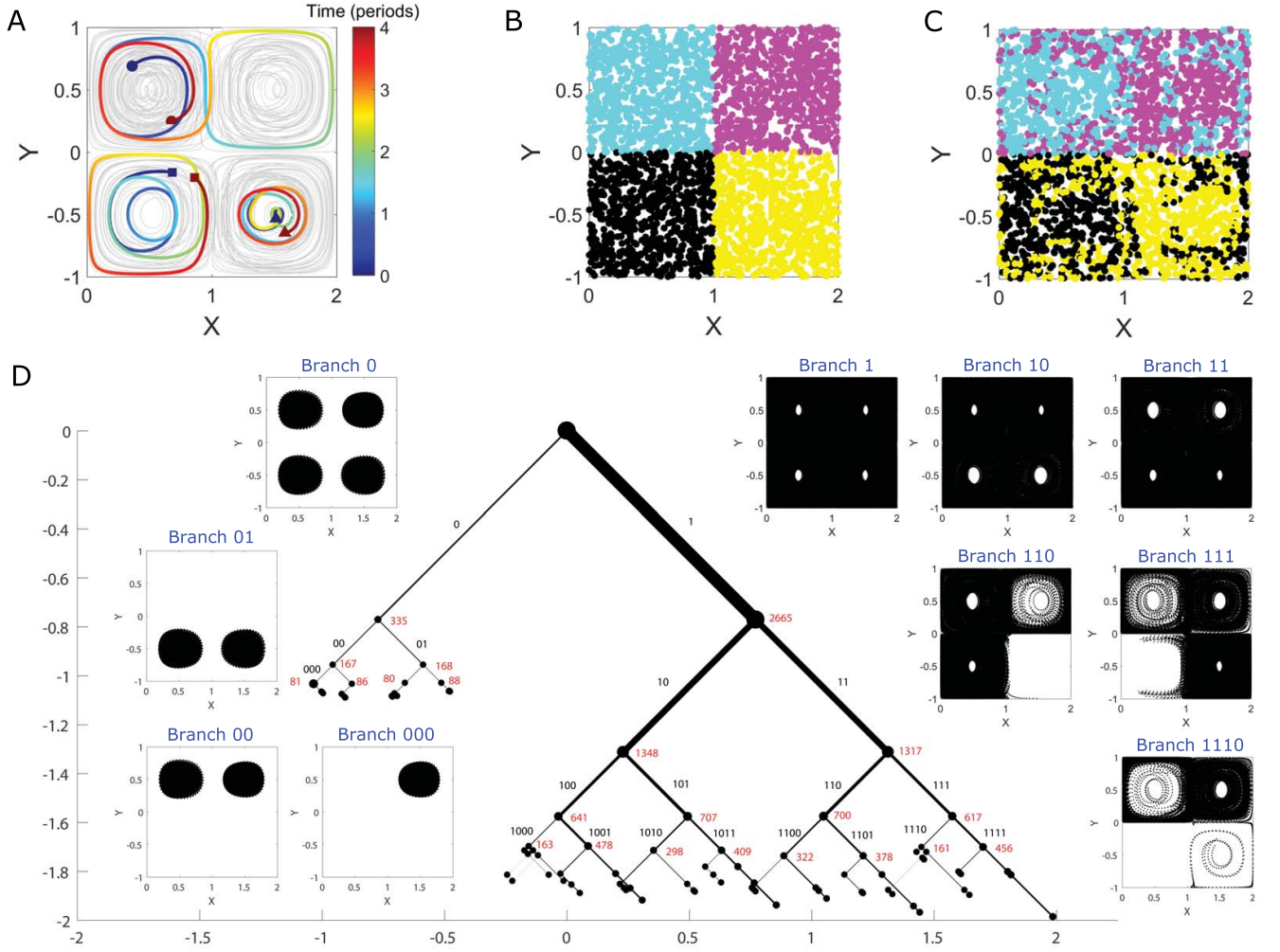


FIG. 3. Quadruple-eddy ocean flow model. (A) Trajectories of 50 selected drifters randomly initialized in the flow (gray). The trajectories of 3 drifters are highlighted for 4 periods of horizontal oscillation, from their initial positions (blue) to their final positions (red). These drifters illustrate qualitatively different trajectories in the flow, including those that switch quadrants (dots), those that remain in a single eddy core (triangles), and those that spiral radially between the center and the boundary of a quadrant (squares). In panel (B), the initial positions of 3000 randomly initialized drifters are colored according to their initial quadrant in the flow. The drifters maintain their color assignment in panel (C), showing how the unsteady eddy motion leads to mixing of the drifters after the 4 periods of horizontal oscillation. The east-west oscillation of the eddy field leads horizontal mixing of the flow. The resulting sCSC dendrogram is shown in panel (D), with every position occupied by all 3000 drifters plotted in black dots in the corresponding inset branch plot. (Note: drifter positions often appear as continuous black patches due to the high density of overlapping positions occupied by the drifters.) The width of each branch is proportional to the fraction of the states that it contains. The corresponding binary code of each branch is labeled in black text, and the number of trajectories associated with each node is labeled in red text. The dendrogram is plotted to the seventh eigenvector, although labels below the fourth eigenvector are omitted for clarity. The horizontal and vertical axes are measured in units of the parameter z , and the branches are plotted at 45-degree angles. We have visualized the first 7 eigenvectors for brevity of presentation, but this does not affect the model results.

ion to simultaneously cluster all of the states. We begin with the most effective partition given by the eigenvector associated with the maximum eigenvalue, and proceed through the set of orthogonal eigenvectors in order of decreasing eigenvalue until the clusters have fully emerged. This approach simultaneously reveals the coherent sets of the system, and eliminates the subjective user inter-

vention required in the previous method¹⁷.

Given a dissimilarity measure and resulting eigenvector solutions, the simultaneous Coherent Structure Coloring (sCSC) algorithm begins by assigning to each state in the system a binary membership based on its corresponding scalar value along each orthogonal coordinate direction. A bifurcation is appropriate given that

each one-dimensional coordinate has two extreme ends toward which the optimization of equation 1 pulls dissimilar states. The states are bifurcated along each coordinate dimension by using agglomerative clustering (although other methods could be used for this step) and assigning to each state a value of 0 or 1 based on its membership within either of the two largest clusters of the resulting dendrogram. Each eigenvector contributes a separate bit to the binary code associated with each of the states in the system, with the leading bit corresponding to the largest eigenvalue and the remaining bits concatenated in decreasing order of their corresponding eigenvalues (figure 2)¹⁹.

The clustering continues through all possible eigenvectors, but a natural stopping criterion emerges from binary splitting. For each subsequent eigenvector, the bifurcation is performed for all data points (i.e. states), and each is assigned a 0 or a 1. For the k th eigenvector bifurcation, this enables 2^k numerically possible clusters. For example, the first splitting produces branches 0 and 1, and the second splitting enables the population of 2^2 unique clusters by appending 0 or 1 to each branch of the existing binary code ($\{00, 01, 10, 11\}$). However, it may be the case that the numerically possible branch 01 is not occupied because there is no data point that receives both a label of 0 in the first bifurcation and a label of 1 in the second bifurcation. Thus, we hypothesize that branch 0 (and its only occupied split, branch 00) evidences a coherent region of the data.

The binary codes generated by the aforementioned process can be visualized in an sCSC dendrogram, with each branch pair connecting those states that differ only at the least significant bit of their binary code. The length of each branch pair is a measure of the dissimilarity between the groups connected by the branches, and it corresponds to the value of the summation in equation 1 computed only over those states connected by the branches. At progressively lower levels of the dendrogram, the corresponding binary codes include bits for progressively smaller eigenvalues. The dissimilarity between the groups connected at lower levels therefore generally becomes smaller as well. As depicted in figure 2, this procedure produces a more informative clustering representation of the example system than the standard approaches in figure 1.

In the next two sections, we apply sCSC to frontier problems in ocean transport and vortex ring formation. Then, to further demonstrate the range of scientific datasets that can be explored with this new method, we use sCSC to achieve an interpretable representation of protein folding.

COHERENT STRUCTURE IDENTIFICATION FROM GEOPHYSICAL FLOW MEASUREMENTS

A key challenge in geophysical fluid dynamics is to extract and characterize coherent fluid motions from the relatively sparsely sampled turbulent flow of air or wa-

ter. The coherent structures, often manifested as eddies and jets, can dominate the transport of heat, salt, nutrients, and pollutants^{20,21}. Therefore, they can serve as the basis for low-order models that capture the salient physics²², or as a template for data assimilation into large-scale weather forecasting models²³. Turbulent flow structures in the ocean also impact the behavior and ecology of marine life²⁴.

Distributed sensor networks such as the Argo collection of 3800 ocean drifters²⁵ sample the flow field in a Lagrangian sense, recording the properties of the water as each drifter is carried by the prevailing currents. Here we demonstrate the unique capability of the sCSC method to extract coherent fluid structures from such collections of Lagrangian measurements. To do so, we first apply sCSC to a common model of Lagrangian ocean drifters in a simplified flow field comprising only four eddies, the unsteady quadruple-eddy flow^{26,27}. While this model represents a simplification of the full physics, it is valuable due to its common use for the evaluation and comparison with existing methods to identify coherent structures^{16,17,26,27}.

As shown in figure 3A, drifter trajectories within the two eddies at the upper-left and lower-right rotate clockwise, whereas trajectories within the other two eddies rotate counter-clockwise. Simultaneous with this rotation, an east-west oscillation of the eddy field occurs, which causes exchange of drifters between the eastern and western eddies. This exchange, which depends on the location and timing of the drifter release relative to the east-west oscillation cycle, is illustrated in the transition from initial drifter positions in figure 3B to their final positions in figure 3C.

Each drifter trajectory represents a state of this fluid dynamic system, and the pairwise dissimilarity between each of the states is given by the standard deviation of the instantaneous distance between drifter positions, divided by the average distance between each pair of drifters¹⁶. This measure anticipates that coherent structures will comprise drifters whose relative positions do not vary as the flow evolves, leading to a small values of the pairwise dissimilarity measure (i.e. a small standard deviation) within each cluster. By contrast, pairs of drifters that straddle the boundary between coherent structures can experience exponential separation over time and correspondingly large standard deviation of their instantaneous separation¹¹.

The sCSC method reveals a clear, physically interpretable structure for this complex flow (figure 3D). The primary bifurcation of the flow is between trajectories that remain in the eddy cores of their original quadrant (Branch 0) and trajectories that do not (Branch 1). The trajectories of Branch 0 are then further subdivided into trajectories that remain within eddy cores in the northern half of the flow (Branch 00) and those that remain within eddy cores in the southern half of the flow (Branch 01), reflecting the absence of north-south drifter exchange. Finally, the trajectories associated with the individual

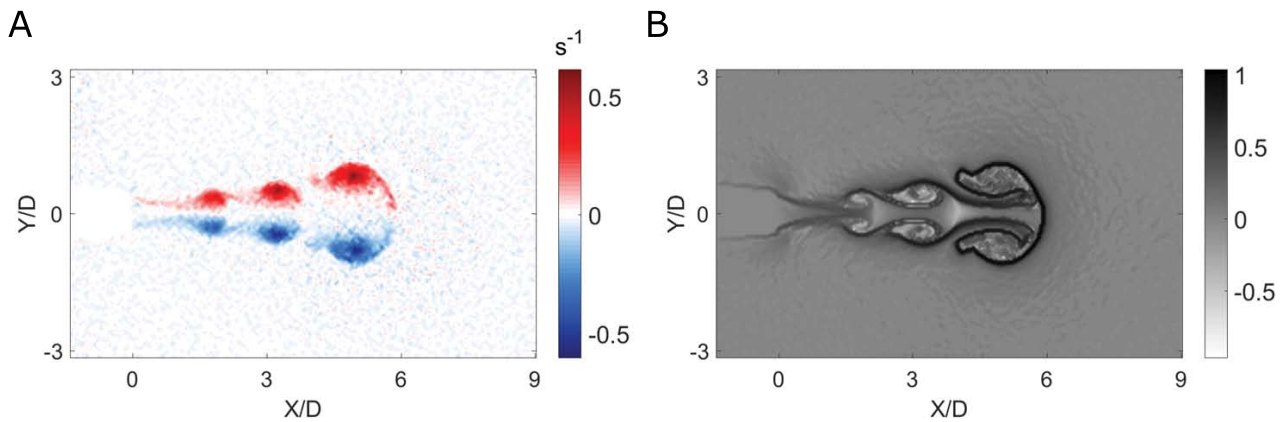


FIG. 4. Empirical measurements of vortex ring formation. (A) Contours of vorticity in the plane of symmetry of a propagating vortex ring. The primary toroidal vortex ring and two toroidal eddies in the trailing jet propagate from left to right. (B) Backward-time FTLE contours computed using 30,500 particles advected in the measured velocity field. The highest FTLE values correspond to an attracting manifold along the interface between the vortex ring and the surrounding fluid. Spatial coordinates are normalized by the cylinder diameter $D = 2.49$ cm.

quadrants are identified at the level of the third bifurcation (e.g. Branch 000 shown in figure 3D inset, as well as Branches 001, 010, and 011 for the other three individual quadrants, not shown in inset).

Whereas the application of k -means clustering or other conventional tools would require a priori guidance to determine that four independent structures exist in branch 0 (i.e. one eddy per quadrant)²⁸, this result is revealed naturally by the sCSC dendrogram, as further bifurcations after Branch 000 do not produce additional coherent states; all of the trajectories that remain together after the third bifurcation remain together after subsequent bifurcation.

To be sure, the presence of the four eddy cores can also be revealed by a contour map of the largest finite-time Lyapunov exponent (FTLE) corresponding to the quadruple-eddy velocity field (see¹⁶ and figure S1 in the SI Appendix). The key advantage of the sCSC approach is that a similar result can be achieved with two orders-of-magnitude less data: FTLE calculations of this flow require release and tracking of 65,000 drifters in order to ensure that the gradient calculation inherent in the FTLE is well-posed. By contrast, the same cores can be identified by as few as 300 drifters using the present method (SI Appendix figure S1), and the cores can be identified as long as drifters are present in the cores over timescales longer than the eddy turnover time.

The structure of branch 1 is less well organized and reflects the chaotic advection of trajectories that spiral radially within a quadrant and/or switch quadrants in the unsteady flow. Nonetheless, the dendrogram structure does indicate geometric symmetries within the chaotic motions, such as a preference for three quadrants among the trajectories in branches 110 and 111; and a more constrained preference for two quadrants exists at branch 1110. A general observation is that geometric symmetries appear as balanced dendrogram bifurcations. This

is in contrast to the structure of random noise, which is characterized by a trivial sCSC dendrogram with a single branch that contains nearly all of the states and a splintering of a small number of fully-converged states at each level of the dendrogram (see figure S2 in the SI Appendix).

EMPIRICAL MEASUREMENT OF VORTEX RING FORMATION AND ENTRAINMENT

Vortex ring formation is a prominent phenomenon in engineered and biological systems as diverse as aerodynamic flow control, animal swimming, and the human cardiovascular system^{29–31}. The growth and dynamics of vortex rings are dictated by the extent to which they entrain surrounding fluid³². Moreover, knowledge of the precise region of the flow that is ultimately entrained by a forming vortex ring can be used to predict how a vortex delivers mass, momentum, and energy to the surrounding flow. For example, pathological vortex ring formation in the human left ventricle has been shown to provide an effective diagnostic of heart failure³¹. Despite the importance of vortex ring entrainment, methods to quantify the region of the flow impacted by vortex rings have shown limited success, particularly in cases for which the finite-time Lyapunov exponent field cannot be calculated due to the sparsity of measurements. Here, we demonstrate the ability of the sCSC technique to precisely identify the region of a flow that is entrained by a forming vortex ring, knowledge that has been previously inaccessible in cases where measurement data is sparse, such as when the flow is interrogated using non-invasive clinical methods such as ultrasound or magnetic resonance imaging.

Vortex rings were formed in the laboratory using a piston-cylinder apparatus described in previous work³³. A motor-driven piston pushes water through a vertical

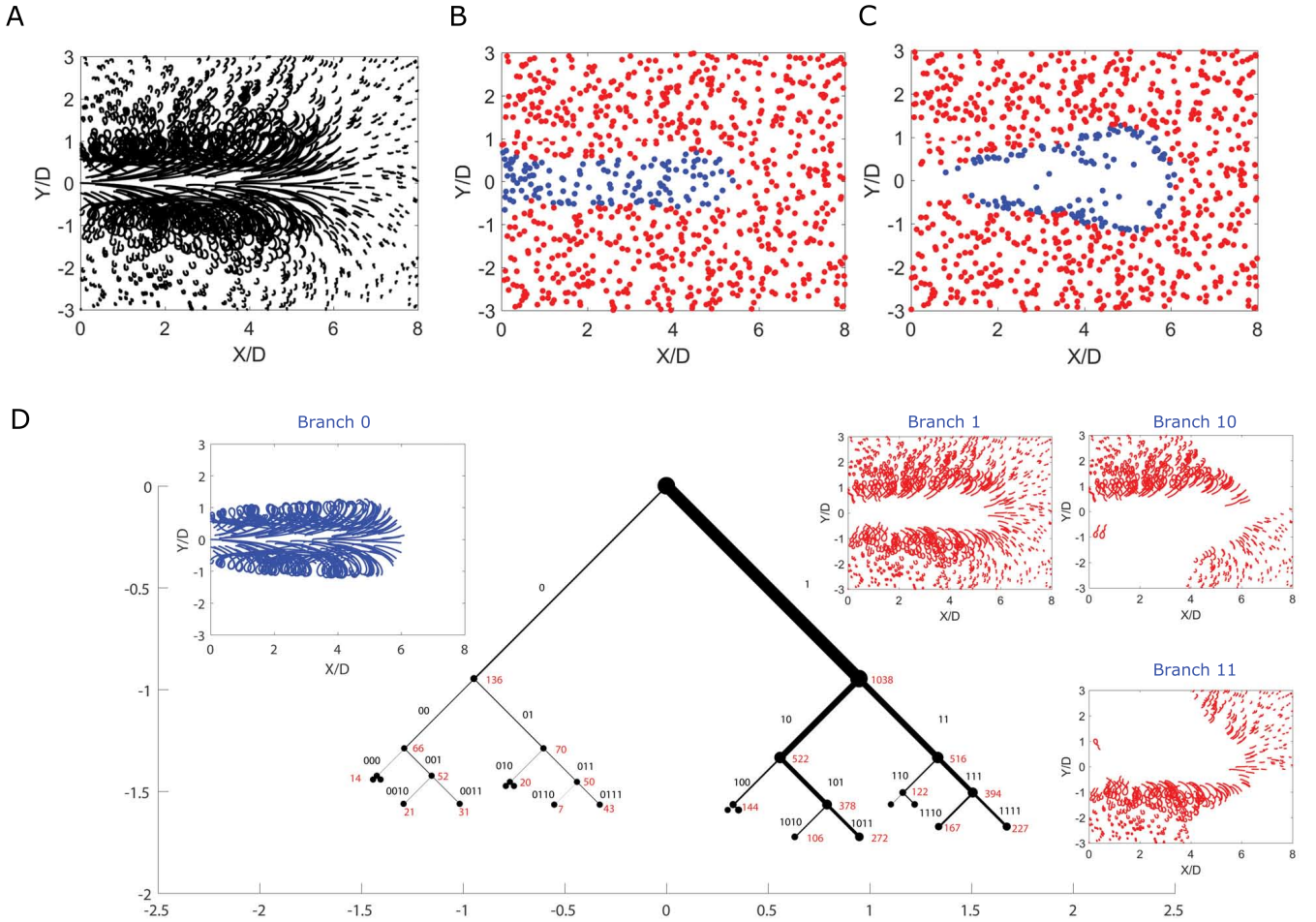


FIG. 5. sCSC analysis of vortex ring formation. (A) Trajectories of 1174 Lagrangian particles initialized in the flow. (B) Initial positions of the 1174 particles. Blue particles are those revealed by the sCSC analysis to be entrained by the vortex ring; red particles are not entrained. (C) Final positions of the same particles tracked in panel B. The sCSC dendrogram on which this analysis is based is shown in panel (D), with every position occupied by all 1174 particles plotted in the corresponding inset branch plot. The width of each branch is proportional to the fraction of the states that it contains. The corresponding binary code of each branch is labeled in black text, and the number of trajectories associated with each node is labeled in red text. The dendrogram is plotted to the fourth eigenvector, although many of the labels are omitted for clarity. The horizontal and vertical axes are measured in units of the parameter z , and the branches are plotted at 45-degree angles. We have visualized the first 4 eigenvectors for brevity of presentation, but this does not affect the model results.

hollow cylinder of diameter $D = 2.49$ cm that is submerged in a tank with cross-sectional area of 61 cm by 61 cm and height of 91 cm. As the flow exits the cylinder at a nominal speed of 7 cm s^{-1} , the fluid boundary layer at the inner surface of the cylinder rolls up into a toroidal vortex ring, which propagates away from the cylinder via self-induction.

Figure 4 plots the vorticity field (panel A) and the backward-time, attracting FTLE field (panel B) of a vortex ring (propagating from left to right in this orientation) measured in its symmetry plane using digital particle image velocimetry³³. The appearance of distinct vorticity patches above and below the axis of symmetry at $Y/D = 0$ is an artifact of the two-dimensional mea-

surement of what is in fact a three-dimensional toroidal structure. This example highlights the fact that distinct regions of vorticity are not necessarily independent coherent structures. The red and blue regions in Fig. 4A are connected by azimuthal vortex loops that emerge perpendicular to the measurement plane.

A set of 1174 fluid particle trajectories in the domain encountered by the vortex ring were analyzed using the present sCSC method to identify regions of the ambient flow that were entrained by the vortex ring. As illustrated in Fig. 5A, it is impossible to determine which fluid particles have been entrained by the vortex ring based on visual inspection of the trajectories alone. Moreover, unlike the FTLE calculation in Fig. 4B based on 30,500 ad-

vected particles, the 1174 trajectories are not sufficiently close to one another to compute the FTLE field, because the required gradient calculations are not well-posed for sparse trajectories. Finally, existing techniques based on heuristics such as k -means or the spectral eigengap rely on knowledge of the number of eddies to guide clustering; in the present case, the individual vorticity patches in Fig. 4A are only tangentially related to the entrainment process³², and it is also unclear whether one should consider the flow to be composed of six eddies (i.e. corresponding to the number of distinct patches of vorticity), three eddies (i.e. corresponding to the number of toroidal vortex structures), or one combined flow structure.

The sCSC dendrogram (Fig. 5D) avoids the need for explicit determination of the number of eddies, as it unambiguously identifies the fluid particles entrained by the vortex ring as those belonging to Branch 0. Branch 1 identifies all other particles and further bifurcations of that branch reveal underlying geometric symmetries, as in Branch 1 of the quadruple-eddy flow in Fig. 3D.

Plots of the initial and final positions of the fluid particles in Fig. 5B and C show that the fluid entrained by the vortex ring occupies a well-defined region in the immediate path of the vortex ring, a result that is consistent with intuition but that can now be characterized quantitatively for the first time. The void created by the evolution of the blue particles from Fig. 5B to Fig. 5C is filled by the fluid ejected from the cylinder. The entrained blue particles ultimately occupy positions around the vortex ring that are consistent with the FTLE analysis shown in Fig. 4B. This provides another demonstration of the interpretability of the sCSC results. Notably, these results have been achieved without any of the ad hoc assumptions required by existing methods of entrainment quantification^{32,34}.

BEYOND FLUIDS: MACROSTATE MODELING OF MOLECULAR DYNAMICS

Whereas fluid dynamics datasets typically represent only a few spatiotemporal coordinates, molecular dynamics datasets can contain thousands of degrees of freedom with complex relationships. We now demonstrate the use of sCSC to analyze a dataset that is more difficult to understand intuitively: the atomistic dynamics of protein folding. Molecular dynamics (MD) simulations of proteins and other biomolecules are performed at the atom level, and their dynamics are modeled as Newtonian. While more advanced theory is often preferred to model reactions in which bonds are made or broken, the Newtonian approximation is well-suited for studies of protein folding or conformational change.

While MD is resource-intensive, advances in simulation parameters³⁵, bespoke hardware³⁶, and distributed computing frameworks³⁷, have enabled MD analyses to yield insight into complex biophysical systems at biologically meaningful timescales. Thus, these simulations have the

potential to uncover the misfolding mechanisms involved in a variety of diseases, to elucidate stable configurations yet undiscovered by crystallography, and to reveal small molecule binding sites and kinetics for drug discovery. However, without complementary analysis methods designed to communicate statistically rigorous and understandable conclusions resulting from such computational experiments, the benefits of advances in MD cannot be fully realized. The use of unsupervised learning to identify meaningful patterns within data, such as metastable states or coherent structures, is vital to leveraging the benefits of high resolution *in silico* analyses.

For this study we use an ultralong MD simulation performed by Lindorff-Larsen et al.³⁸ of the folding and unfolding of Protein G, a 56-residue protein expressed in streptococcal bacteria. The simulation details are described in the Supporting Materials of³⁸. To define the states of the system, we use a Markov state model (MSM) analysis, which codifies the system using a kinetic master equation³⁹. This master equation takes the form of a microstate transition matrix, in which each microstate is identified by a probability distribution of transitioning to every other microstate. Ultimately, we are interested in clustering these microstates into a smaller number of interpretable macrostates, since it is conceptually difficult to describe hundreds of unique microstates in a physically interpretable way⁴⁰.

The MSM transition probability matrix is constrained to be stochastic, symmetric with respect to a stationary distribution, ergodic, and aperiodic. It can thus be decomposed into eigenvalues and eigenvectors, $T(\tau)\lambda = \psi\lambda$, where the eigenvalues are on the unit interval $|\lambda_i| \leq 1$ and the highest eigenvalue $\lambda_1 = 1$ is unique. The variational principle states that the sum of estimated eigenvalues is bounded from above by the sum of true eigenvalues. Thus, many state decompositions can be tested according to the sum of a set number of eigenvalues for a set Markovian lag time, and the state decomposition resulting in the highest sum of approximated eigenvalues can be chosen for further analysis. For our MSM, we found that 175 microstates optimally describes the system according to a variational evaluation. The MSM construction protocol is consistent with current best practices and is described in the Methods.

Several algorithms exist to coarse-grain a microstate transition matrix, and these provide a basis for evaluating the results of sCSC. Perron cluster-cluster analysis (PCCA)⁴¹ utilizes the eigendecomposition of the transition matrix and determines macrostates using the dominant eigenvectors. It is similar to the approach used in principal direction divisive clustering (PDDC)⁹, exhibits the same limitations of divisive clustering previously discussed, and has been shown to produce less effective models for this reason⁴². Although both PCCA and sCSC utilize the eigenvector elements from a matrix decomposition, the similarity is only superficial because the decomposed matrices represent different aspects of the system (adjacency and transition probabilities, respec-

tively). More recent approaches have quantified pairwise microstate adjacency using information theory, and then perform hierarchical agglomerative clustering^{42,43}. However, agglomerative clustering is conceptually similar to divisive clustering in that data points cannot be assigned to different clusters once agglomerated, which impairs the ability of the method to capture orthogonal processes.

We leverage the aforementioned information theory-inspired methods to quantify adjacency, but use sCSC to determine macrostates instead of agglomerative hierarchical clustering. If two microstates are defined by transition probability distributions P and Q , their pairwise dissimilarity can be written using the Jensen-Shannon divergence¹²,

$$\text{div}_{JS}(P||Q) = \frac{1}{2} \sum_i P_i \log \frac{P_i}{M_i} + \frac{1}{2} \sum_i Q_i \log \frac{Q_i}{M_i} \quad (3)$$

where M is the elementwise mean of P and Q , and each term is the Kullback-Leibler divergence to the mean. We quantify the dissimilarity between microstates using the square root of equation 3^{42,44}. We then create an sCSC dendrogram using this definition of adjacency (figure 6). Nine branches of the sCSC dendrogram are depicted by sampling one structure from each microstate contained in that branch. In total, the nine depicted branches contain all 175 original microstates. By superimposing a representative conformation from each microstate and coloring the protein according to its secondary structure, we can interpret the sCSC groupings.

First, we note that the folded state (Branch 0) is identified in the first sCSC solution and is separated from the denatured, unfolded ensemble, which comprises the rest of the dendrogram (Branch 1). We see that the folded state is a well-defined conformation with small variance across sampled structures. The incorporation of subsequent sCSC eigenvectors identifies groups of structures unified by their protein secondary structure features. Various branches contain similar secondary structure elements, elucidating substructures exhibited during the folding of Protein G. For example, Branch 1110 contains β -sheet secondary structure (yellow), whereas Branch 11110 contains noticeable α -helical secondary structure (pink). Branch 111111 is the least coherent, containing the most unstructured microstates. Summary statistics for each macrostate can be found in Table S1 in the SI Appendix.

In this example, we have chosen to highlight secondary structure changes so we can understand which secondary structure elements characterize different subprocesses within folding. We see that the yellow β -sheet secondary structure appears in several macrostates—often along with the blue 3_{10} -helix, thought to be an intermediate structure during α -helix formation⁴⁵—which might indicate that the formation of the pink α -helix is a rate-limiting step in the folding process. However, we could also choose to quantify and visualize macrostate contact maps, radii of gyration, or distance to various structures in order to gain complementary insight into the folding system. For other dynamical processes found in proteins, such as conformational change, allostery, and drug binding, we might choose to visualize parameters related to specific sites of interest or observables that can be probed experimentally. The choice of how to describe the macrostates is independent of the clustering process, but the depictions or statistics that enable the best interpretation of the system will depend on the dynamics of interest.

The sCSC dendrogram analysis offers advantages in the interpretation of protein folding that exceed the current state of the art and avoid the difficulties of standard clustering algorithms. First, a hierarchical representation of structural motifs according to the extent of their dissimilarity provides insight into the protein conformations that characterize subprocesses within folding. Second, truncating the dendrogram when bifurcations are unoccupied produces an objective way to visualize the converged clusters. Third, the generation of orthogonal sCSC solutions enables orthogonal dynamical processes in the protein folding simulation to be incorporated in analogy to the simple model in figure 2. We thus anticipate that this type of interpretable macrostate model for atomistic protein folding dynamics will be transformative in the study of biophysical and other processes governed by equilibrium molecular dynamics.

DISCUSSION

The present approach addresses the previously stated challenges with common clustering algorithms: it does not require a choice of cluster number or dendrogram cutting, it maintains a hierarchical relationship among splittings without restricting divisions to a single cluster, and it leverages the concept of dissimilarity in a computationally tractable way.

Perhaps the most important advantage of this approach relative to commonly used tools is that the number, shape, and size of clusters in the data emerges naturally from the sCSC dendrogram rather than being specified a priori. As the set of eigenvectors that is included in the analysis is increased to include those associated with lesser eigenvalues, the number of unoccupied binary codes generally increases. This is because progressively fewer groups of states that survived the preceding orthogonal partitions will be subsequently separated at lower levels of the dendrogram. In this way, the set of clusters in the dataset is revealed to be those branches of the dendrogram structure whose shape converges as the number of eigenvectors included in the analysis increases. The sCSC dendrogram indicates not only the number of these converged clusters but also the relative strength of the partitions between clusters, via the length of the connecting branches in z -space.

Unlike agglomerative clustering, small differences between states at lower levels of the sCSC dendrogram have no impact on the clusters that form at higher levels, as the top-down approach begins by using the most significant partitions indicated by the eigenvectors associated with the largest eigenvalues. Furthermore, because the sCSC dendrogram structure is determined in one step by the simultaneous use of all of the eigenvectors, the computational complexity and combinatorial limitations of existing divisive hierarchical clustering techniques⁶ or multi-pass clustering algorithms is avoided. This facilitates application to larger datasets.

The scientific applications presented here have been selected to demonstrate the wide diversity of datasets that can be explored using the sCSC method. These include equilibrium or nonequilibrium systems, experimental or computational studies, and rich or sparse datasets. Domain knowledge should inform selection of an appropriate dissimilarity measure, but ad hoc and a priori assumptions about the structure of the data itself are not needed. We anticipate that these features will make sCSC a powerful tool for interrogating both new and longstanding research problems, including those in fields where the underlying processes are less accessible, such as genomics and neuroscience. For example, genetic ancestries can potentially be clustered on the basis of the sCSC structure that emerges from the dissimilarity of single-nucleotide polymorphisms (SNPs) among individuals within a population. In the latter case, differences in neuronal activation can be amplified using sCSC to identify emergent functions that involve coor-

dination of spatially distant neurons. These and other applications can be pursued immediately given the tools developed here. Example MATLAB and Python codes, including a Jupyter notebook tutorial, are available at <https://dabirilab.com/software>.

METHODS

Quadruple-eddy ocean flow model. The velocity field of the quadruple-eddy ocean flow model is given by,

$$\begin{aligned}\frac{dx}{dt} &= -\pi A \sin(\pi f) \cos(\pi y) \\ \frac{dy}{dt} &= -\pi A \cos(\pi f) \cos(\pi y)(2ax + b),\end{aligned}$$

where $x = [0, 2]$ and $y = [-1, 1]$ are the dimensionless east-west and north-south spatial coordinates (i.e. normalized by the quadrant side length), t is time in dimensionless units, and

$$\begin{aligned}a &= \epsilon \sin(\omega t) \\ b &= 1 - 2\epsilon \sin(\omega t) \\ f &= ax^2 + bx.\end{aligned}$$

In the present unsteady implementation of the model, $A = 0.1$, $\epsilon = 0.1$, and $\omega = 2\pi/10$. 3000 Lagrangian drifters were randomly initialized in the domain and advected in the flow using a fifth-order Runge-Kutta integration scheme. The duration of advection was 40 dimensionless time units, corresponding to 4 periods of horizontal oscillation of the flow.

Markov state models. Markov state models (MSMs) are a kinetic master equation framework for describing and analyzing time-series data such as molecular dynamics (MD) simulations. A MSM requires partitioning the phase space explored by a system into discrete states, and is represented by a transition probability matrix defined for a Markovian lag time τ at which transitions between the states are independent of the history of the system. For protein folding analyses, phase space (positions and velocities) is conventionally approximated by conformation space (positions), and states are chosen according to an objective optimization protocol, in this case a variational principle⁴⁶. The Markovian lag time chosen to analyze a system must be long enough for memoryless inter-state transitions, but short enough to resolve dynamics; for protein folding dynamics, lag times on the order of tens of nanoseconds are typical. The MSM transition probability matrix is constrained to be stochastic, symmetric with respect to a stationary distribution, ergodic, and aperiodic. It can thus be decomposed into eigenvalues and eigenvectors, $T(\tau)\lambda = \psi\lambda$, where the eigenvalues are on the unit interval $|\lambda_i| \leq 1$ and the highest eigenvalue $\lambda_1 = 1$ is unique. The variational principle states that the sum of estimated eigenvalues is bounded

from above by the sum of true eigenvalues; thus many state decompositions can be tested according to the sum of a set number of eigenvalues for a set Markovian lag time and the state decomposition resulting in the highest sum of approximated eigenvalues can be chosen for further analysis.

The MSM for the simulation analyzed in this work was constructed according to the protocol used in⁴⁷ for a set lag time of 50 ns according to a previous analysis for the same system performed by⁴⁸. First, the Cartesian coordinates from the raw simulation data are transformed into the sines and cosines of the ϕ and ψ side chain dihedral angles for each amino acid of the protein. Then, the vector of dihedrals is again transformed using time structure-based independent component analysis (tICA)⁴⁹ with a tICA lag time of 50 ns wherein each tICA solution vector was weighted according to its associated eigenvalue⁵⁰. Then, mini-batch k -means was used to cluster the simulation frames according to their weighted tICA representations for 265 different numbers of cluster centers randomly chosen between 10 and 5000. Finally, a MSM was constructed on each k -means state decomposition in which the transition probability matrix is obtained using a maximum likelihood estimator of the data such that detailed balance is achieved. For each model, five MSMs were fit to a randomly chosen half of the data and then applied to the other half of the data, and the latter was used to sum the first 50 MSM eigenvalues as that model's score. The winning model was chosen to be the one that achieved the single maximum score from parameter sets with mean scores within one standard deviation of the maximum mean score. For our analysis of 265 different microstate numbers, the best model according to this variational analysis had 175 microstates and was used for analysis in the main text.

Software. Example MATLAB and Python codes, including a Jupyter notebook tutorial, are available at <https://dabirilab.com/software>.

AUTHOR CONTRIBUTIONS

B.E.H. and J.O.D. designed the experiments and performed the analysis. K.L.S.-K. and J.O.D. performed the fluid dynamics simulation and obtained the experimental dataset. B.E.H. and J.O.D. visualized results, formulated conclusions, and wrote the manuscript. J.O.D. supervised the research.

ACKNOWLEDGMENTS

The authors are grateful to Muneeb Sultan, Jared Dunnmon, Nicole Xu, and the referees for insightful manuscript feedback and to D. E. Shaw Research for providing the Protein G dataset. This work was supported

by the U.S. National Science Foundation and by the Department of Defense (DoD) through the National Defense Science & Engineering Graduate Fellowship (NDSEG) Program.

- ¹U. von Luxburg, R. C. Williamson, and I. Guyon, “Clustering: Science or art?” in *Proceedings of ICML Workshop on Unsupervised and Transfer Learning*, Proceedings of Machine Learning Research, Vol. 27, edited by I. Guyon, G. Dror, V. Lemaire, G. Taylor, and D. Silver (PMLR, Bellevue, Washington, USA, 2012) pp. 65–79.
- ²J. Macqueen, “Some methods for classification and analysis of multivariate observations,” in *5th Berkeley Symposium on Mathematical Statistics and Probability* (1967) pp. 281–297.
- ³J. C. Dunn, “A fuzzy relative of the isodata process and its use in detecting compact well-separated clusters,” *J. Cybern.* **3**, 32–57 (1973).
- ⁴M. Ester, H.-P. Kriegel, J. Sander, and X. Xu, “A density-based algorithm for discovering clusters in large spatial databases with noise,” in *Proceedings of the Second ACM SIGKDD International Conference on Knowledge, Discovery, and Data Mining*, Vol. 96 (1996) pp. 226–231.
- ⁵M. E. J. Newman and M. Girvan, “Finding and evaluating community structure in networks,” *Phys. Rev. E* **69**, 026113 (2004).
- ⁶L. Kaufman and P. J. Rousseeuw, *Finding groups in data: an introduction to cluster analysis*, Vol. 344 (John Wiley & Sons, 2009).
- ⁷D. Xu and Y. Tian, “A comprehensive survey of clustering algorithms,” *Ann. Data Sci.* **2**, 165–193 (2015).
- ⁸T. Ali, S. Asghar, and N. A. Sajid, “Critical analysis of db-scan variations,” in *2010 International Conference on Information and Emerging Technologies* (2010) pp. 1–6.
- ⁹D. Boley, “Principal direction divisive partitioning,” *Data Min. Knowl. Discov.* **2**, 325–344 (1998).
- ¹⁰J. Guckenheimer and P. Holmes, *Nonlinear Oscillations, Dynamical Systems, and Bifurcations of Vector Fields*, Vol. 42 (Springer, 1983).
- ¹¹G. Haller and G. Yuan, “Lagrangian coherent structures and mixing in two-dimensional turbulence,” *Physica D* **147**, 352–370 (2000).
- ¹²J. Lin, “Divergence measures based on the Shannon entropy,” *IEEE Transactions on Information Theory* **37**, 145–151 (1991).
- ¹³K. M. Hall, “An r-dimensional quadratic placement algorithm,” *Management Sci.* **17**, 219–229 (1970).
- ¹⁴This maximization is expressed using the Lagrangian form, see¹⁶ for more details.
- ¹⁵S. Munoz, M. T. Ortuno, J. Ramirez, and J. Yanez, “Coloring fuzzy graphs,” *Omega* **33**, 211–221 (2005).
- ¹⁶K. L. Schlueter-Kuck and J. O. Dabiri, “Coherent structure colouring: identification of coherent structures from sparse data using graph theory,” *J. Fluid Mech.* **811**, 468–486 (2017).
- ¹⁷K. L. Schlueter-Kuck and J. O. Dabiri, “Identification of individual coherent sets associated with flow trajectories using coherent structure coloring,” *Chaos* **27**, 091101 (2017).
- ¹⁸W. H. Press, S. A. Teukolsky, W. T. Vetterling, and B. P. Flannery, *Numerical Recipes* (Cambridge University Press, 2007).
- ¹⁹Though we suggest using a bifurcation in general, the method does not prohibit the division of each eigenvector coordinate into three or more discrete bins, thus creating a k -way splitting and associated base- k codes.
- ²⁰F. Huhn, A. von Kameke, V. Perez-Munuzuri, M. J. Olascoaga, and F. Beron-Vera, “The impact of advective transport by the south indian ocean countercurrent on the madagascar plankton bloom,” *Geophys. Res. Lett.* **39**, L06602 (2012).
- ²¹C. W. Hughes and P. I. Miller, “Rapid water transport by long-lasting modon eddy pairs in the southern midlatitude oceans,” *Geophys. Res. Lett.* (2017).
- ²²E. Kaiser, B. R. Noack, L. Cordier, A. Spohn, M. Segond, M. Abel, G. Daviller, J. Osth, S. Krajnovic, and R. K. Niven, “Cluster-based reduced-order modelling of a mixing layer,” *J. Fluid Mech.* **754**, 365–414 (2014).
- ²³J. Maclean, N. Santitissadeekorn, and C. K. Jones, “A coherent structure approach for parameter estimation in lagrangian data assimilation,” *Physica D* **360**, 36–45 (2017).
- ²⁴A. Sengupta, F. Carrara, and R. Stocker, “Phytoplankton can actively diversify their migration strategy in response to turbulent cues,” *Nature* **543**, 555–558 (2017).
- ²⁵Argo, Argo float data and metadata from Global Data Assembly Centre (Argo GDAC) (2000).
- ²⁶M. R. Allshouse and T. Peacock, “Lagrangian based methods for coherent structure detection,” *Chaos* **25**, 097617 (2015).
- ²⁷G. Froyland and K. Padberg-Gehle, “A rough-and-ready cluster-based approach for extracting finite-time coherent sets from sparse and incomplete trajectory data,” *Chaos* **25**, 087406 (2015).
- ²⁸A. Hadjighasem, M. Farazmand, D. Blazeviski, G. Froyland, and G. Haller, “A critical comparison of lagrangian methods for coherent structure detection,” *Chaos* **27**, 053104 (2017).
- ²⁹P. S. Krueger and M. Gharib, “The significance of vortex ring formation to the impulse and thrust of a starting jet,” *Phys. Fluids* **15**, 1271–1281 (2003).
- ³⁰J. O. Dabiri, “Optimal vortex formation as a unifying principle in biological propulsion,” *Annu. Rev. Fluid Mech.* **41**, 17–33 (2009).
- ³¹M. Gharib, E. Rambod, A. Kheradvar, D. J. Sahn, and J. O. Dabiri, “Optimal vortex formation as an index of cardiac health,” *Proc. Natl. Acad. Sci. USA* **103**, 6305–6308 (2006).
- ³²J. O. Dabiri and M. Gharib, “Fluid entrainment by isolated vortex rings,” *J. Fluid Mech.* **511**, 311–331 (2004).
- ³³K. L. Schlueter-Kuck and J. O. Dabiri, “Pressure evolution in the shear layer of forming vortex rings,” *Phys. Rev. Fluids* **1**, 012501(R) (2016).
- ³⁴A. B. Olcay and P. S. Krueger, “Measurement of ambient fluid entrainment during vortex ring formation,” *Exp. Fluids* **44**, 235–247 (2008).
- ³⁵L.-P. Wang, K. A. McKiernan, J. Gomes, K. A. Beauchamp, T. Head-Gordon, J. E. Rice, W. C. Swope, T. J. Martínez, and V. S. Pande, “Building a more predictive protein force field: A systematic and reproducible route to amber-fb15,” *J. Phys. Chem. B* **121**, 4023–4039 (2017).
- ³⁶D. E. Shaw, P. Maragakis, K. Lindorff-Larsen, S. Piana, R. O. Dror, M. P. Eastwood, J. A. Bank, J. M. Jumper, J. K. Salmon, Y. Shan, and W. Wrighers, “Atomic-level characterization of the structural dynamics of proteins,” *Science* **330**, 341–346 (2010).
- ³⁷M. Shirts and V. S. Pande, “Screen savers of the world unite!” *Science* **290**, 1903–1904 (2000).
- ³⁸K. Lindorff-Larsen, S. Piana, R. O. Dror, and D. E. Shaw, “How fast-folding proteins fold,” *Science* **334**, 517–520 (2011).
- ³⁹B. E. Husic and V. S. Pande, “Markov state models: From an art to a science,” *J. Am. Chem. Soc.* **140**, 2386–2396 (2018).
- ⁴⁰V. S. Pande, K. Beauchamp, and G. R. Bowman, “Everything you wanted to know about markov state models but were afraid to ask,” *Methods* **52**, 99–105 (2010).
- ⁴¹P. Deuffhard, W. Huisinga, A. Fischer, and C. Schütte, “Identification of almost invariant aggregates in reversible nearly uncoupled Markov chains,” *Linear Algebra Appl.* **315**, 39–59 (2000).
- ⁴²B. E. Husic, K. A. McKiernan, H. K. Wayment-Steele, M. M. Sultan, and V. S. Pande, “A minimum variance clustering approach produces robust and interpretable coarse-grained models,” *J. Chem. Theor. Comput.* (2017).
- ⁴³G. R. Bowman, “Improved coarse-graining of markov state models via explicit consideration of statistical uncertainty,” *J. Chem. Phys.* **137**, 134111 (2012).
- ⁴⁴D. M. Endres and J. E. Schindelin, “A new metric for probability distributions,” *IEEE Transactions on Information Theory* **49**, 1858–1860 (2003).
- ⁴⁵M. Sundaralingam and Y. Sekharudu, “Water-inserted α -helical segments implicate reverse turns as folding intermediates,” *Science* **244**, 1333–1337 (1989).
- ⁴⁶F. Noé and F. Nüske, “A variational approach to modeling slow processes in stochastic dynamical systems,” *Multiscale Model.*

- Simul. **11**, 635–655 (2013).
- ⁴⁷B. E. Husic and V. S. Pande, “Ward clustering improves cross-validated Markov state models of protein folding,” J. Chem. Theory Comput. **13**, 963–967 (2017).
- ⁴⁸K. A. Beauchamp, R. McGibbon, Y.-S. Lin, and V. S. Pande, “Simple few-state models reveal hidden complexity in protein folding,” Proc. Natl. Acad. Sci. **109**, 17807–17813 (2012).
- ⁴⁹C. R. Schwantes and V. S. Pande, “Improvements in Markov state model construction reveal many non-native interactions in the folding of NTL9,” J. Chem. Theory Comput. **9**, 2000–2009 (2013).
- ⁵⁰F. Noé and C. Clementi, “Kinetic distance and kinetic maps from molecular dynamics simulation,” J. Chem. Theory Comput. **11**, 5002–5011 (2015).